Zircon (U-Th)/He thermochronology and thermal evolution of the Tarim Basin, Western China

Jian Chang [a,b,*], Xin Yang [c], Nansheng Qiu [a,b], Kyoungwon Min [d], Chenxing Li [a,b], Huili Li [c], Dan Li [a,b]

[a] State Key Laboratory of Petroleum Resources and Prospecting, China University of Petroleum, Beijing 102249, China
[b] College of Geosciences, China University of Petroleum, Beijing, China
[c] Petroleum Exploration and Production Research Institute, SINOPEC, Beijing 100083, China
[d] Department of Geological Sciences, University of Florida, Gainesville, FL 32611, USA

ARTICLE INFO

ABSTRACT

Thermal history reconstruction of the deep and ancient strata (Pre-Silurian) in the Tarim Basin is always difficult due to the lack of effective paleo-thermal indicators. This study provides a new strategy for thermal history reconstruction of the Tarim Basin with the zircon (U-Th)/He thermochronology. The obvious dispersion of the single-grain zircon (U-Th)/He ages for all the clastic rocks in the Tarim Basin reflects the complex and protracted thermal histories. The combination of forward and inverse modeling revealed that the Neoproterozoic rocks from the Kalpin and Bachu Uplifts experienced four rapid cooling events beginning in the Late Ordovician, Late Carboniferous, Late Triassic and Early Miocene, while the Silurian rocks in the eastern Tarim Basin just experienced the Late Carboniferous and Late Cretaceous cooling events. In addition, these rocks experienced several thermal events with the highest temperature of 160–180 °C (a precision of 5–10 °C). The unique thermal histories in the Tabei Uplift and Shunbei area was suitable for the crude oil preservation. This study not only promotes the application of the zircon (U-Th)/He thermochronology in sedimentary basins but also clarify the thermal evolution process of the ancient strata in the Tarim Basin, which plays an important role in determining the deeper source rocks maturation phase and hydrocarbon occurrence state.

1. Introduction

The Tarim Basin in western China is a petroliferous basin with complex tectonic and sedimentary features. Recently, there have been several oil and gas reservoirs with depths of greater than 6500 m discovered in the Tarim Basin, such as Shunbei, Zhongshen No.1, and Tashen No.1 (Yun and Zhai, 2008; Wang et al., 2014; Jiao, 2018), indicating that the hydrocarbon exploration potential in the deep and ancient formations of the Tarim Basin is very great. The geothermal field plays a major role in hydrocarbon generation and conservation in petroliferous basins. Most studies indicate that present-day conditions of the Tarim Basin are "cool" with an average surface heat flow of ~42.5 mW/m^2 and an average geothermal gradient of ~20.7 °C/km (Wang et al., 1995; Liu et al., 2016). According to numerous borehole temperature and rock thermal physical data, Liu et al. (2016) discussed the temperature distribution at depths of 1000–5000 m, characterized by higher temperatures in the uplift areas and lower temperatures in the

depressions. Multiple studies have primarily examined the Phanerozoic thermal history of the Tarim Basin with vitrinite reflectance, apatite (U-Th)/He, and apatite fission track data (Li et al., 2005, 2010; Ren et al., 2009; Qiu et al., 2010, 2012; Chang et al., 2012a, 2014, 2016, 2017, 2019). However, its Neoproterozoic thermal history has rarely been studied due to the lack of effective thermal indicators. In recent years, zircon (U-Th)/He (hereafter, ZHe) thermochronology has been successfully used to reveal the thermal history of ancient cratons (including the Canadian Shield, Fennoscandian Shield, and Wyoming Craton) since the Paleo-Proterozoic (Orme et al., 2016; Powell et al., 2016; Guenthner et al., 2017; Delucia et al., 2018). This is because the new zircon radiation damage and annealing model (ZRDAAM) developed by Guenthner et al. (2013) can effectively account for the dispersity of single-grain ZHe ages caused by radiation damage and helium diffusion anisotropy. Guenthner et al. (2013) considered that the ZHe closure temperature increases from ~ 140 °C to 220 °C between alpha doses of 10^{16} to 10^{18} α/g. Therefore, it makes sense to accurately reveal the
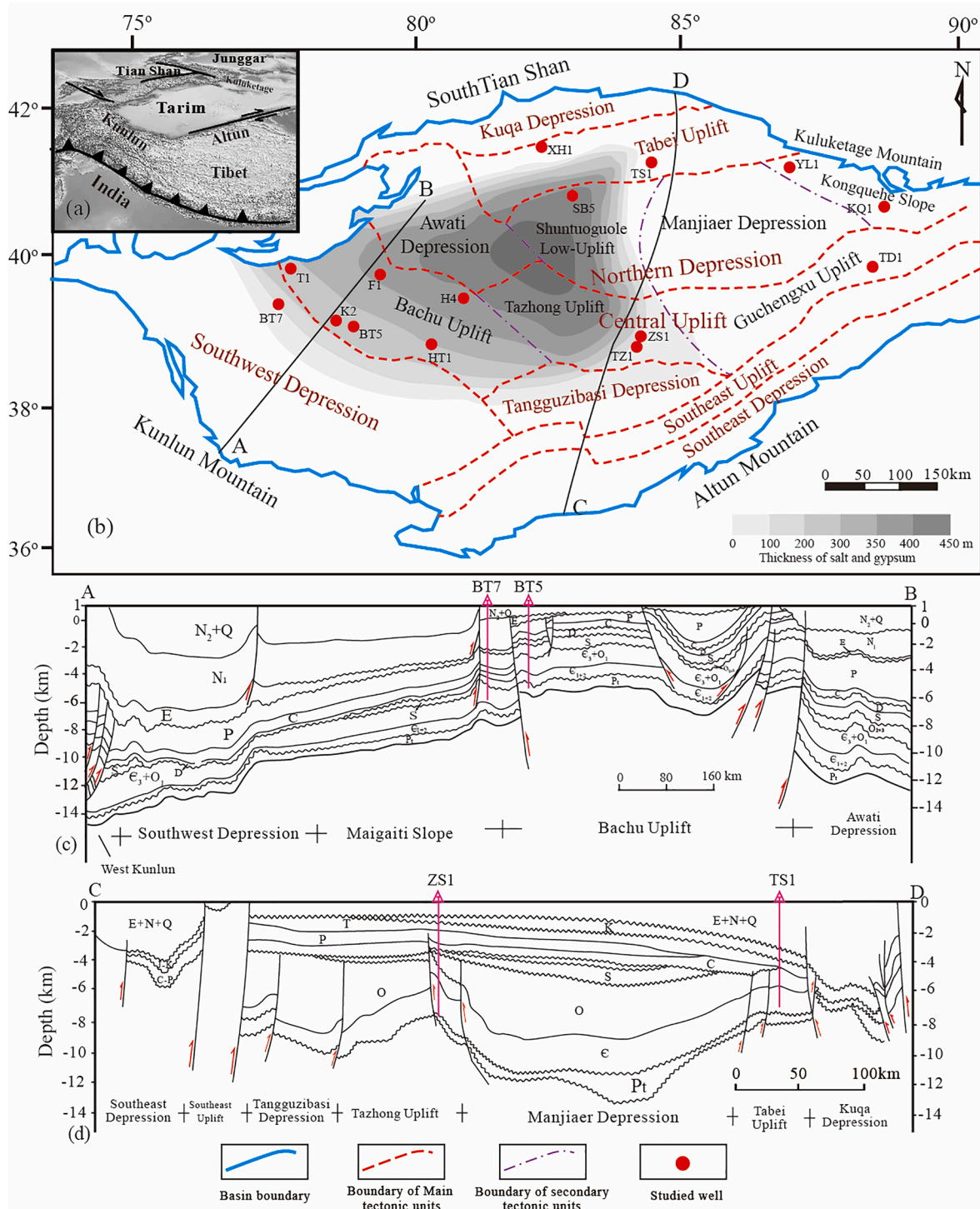
Fig. 1. (a) Schematic map of Central Asia showing the location of the Tarim Basin; (b) Division of the tectonic units in the Tarim Basin (Modified from Jia (1997)) showing the distribution of Middle Cambrian salt and gypsum strata (Yang, 2015) and the studied wells and outcrop; (c) and (d) Typical cross-sections across the Tarim Basin (locations shown in Fig. 1b) with the projections of the studied wells BT7, BT5, ZS1 and TS1. The stratigraphic abbreviations are shown in Fig. 2.

Neoproterozoic thermal history of the Tarim Basin combined with multiple single-grain ZHe ages and new ZRDAAM.

In this study, we first analyze the distribution characteristic of thirty-nine ZHe ages of five rocks collected from the Bachu Uplift, Kalpin Uplift, and Kongquehe Slope in the Tarim Basin, which were then used to carry out forward and inverse modeling for revealing the Neoproterozoic thermal history of the Tarim Basin. Finally, we discuss the thermal simulation effectiveness, the relationship between the cooling events and tectonic events and thermal effects on the deep source rocks and reservoirs. This study provides new insights for how to study the thermal evolution of the basins with zircon (U-Th)/He data, and the reconstructed thermal histories are of significance for understanding the mechanism of tectonic dynamics and petroleum resource assessments in the Tarim Basin and across Central Asia.
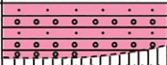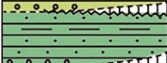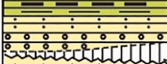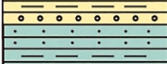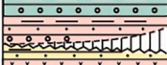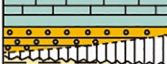
Era	System	Series	Thickness (m)	Age (Ma)	Lithology	K (W/m·k)	A (µW/m³)	Tectonic Movement
Cenozoic	Quaternary (Q)	Holocene	50-1400		Conglomerate, and sandstone			Himalayan
		Pleistocene		2.5				
	Neogene (N)	Pliocene	1200-2300		Conglomerate, Sandstone and mudstone	1.759±0.831	1.724±0.656	
		Miocene		23				
	Paleogene (E)	Oligocene	600-1000		Sandstone and mudstone	1.898±0.624	1.230±0.447	
		Eocene						
		Paleocene		65				
Mesozoic	Cretaceous (K)	Upper	660-1660		Sandstone and mudstone	1.587±0.805	1.380±0.662	Yanshan
		Lower		137				
	Jurassic (J)	Upper	0-2233		Conglomerate, sandstone, siltstone, coal and mudstone	1.736±0.334	2.064±0.999	
		Middle						
		Lower		205				Indosinian
	Triassic (T)	Upper	1173-1991		Sandstone, siltstone and mudstone	2.025±0.389	1.344±0.420	Hercynian stage II
		Middle						
		Lower		250				
Paleozoic	Permian (P)	Upper	1419-2325		Mudstone, siltstone and volcanic rocks	2.135±0.592	1.479±1.051	
		Middle						
		Lower		290				
	Carboniferous (C)	Upper	276-884		Shale and limestone	2.211±0.542	1.282±0.897	Hercynian stage I
		Lower		350				
	Devonian (D)	Upper	215-792		Mudstone and sandstone	2.496±0.671	1.469±1.161	Caledonian Stage III
		Lower+Middle		410				
	Silurian (S)		500-2100		Shale, sandstone	2.457±0.575	1.432±0.723	Caledonian Stage II
				438				
	Ordovician (O)	Upper	1475-4562		limestone, dolomitic limestone, reef, calcarenite	2.562±0.664	0.687±0.668	
		Middle						
		Lower		490				
	Cambrian (Є)	Upper	513-2899		Dolomite, dolomitic limestone, gypsum and mudstone	3.727±0.813	0.406±0.183	Caledonian Stage I
		Middle						
		Lower		543				
Neo-Proterozoic	Edicaran				Dolomite, conglomerate, sandstone, basite, tillite	3.366±1.314	0.554±0.624	Kalpin
	Cryogenian			635				

Fig. 2. General stratigraphic column of the Tarim Basin (modified from Qiu et al. (2012) and Lin et al. (2012). The data of thermal conductivity (K) and heat production (A) were first reported by Liu et al. (2016).

2. Geological setting

The Tarim Basin is the largest in Central Asia, with an area of 56 × 10^4 km^2 and is bounded by the Tian Shan mountain range to the north, the Kuluketage Mountains to the northeast, the Kunlun Mountains to the southwest, and the Altun Mountains to the southeast (Fig. 1a). The Tarim Basin can be divided into eight tectonic units: the Kuqa Depression, Tabei Uplift, Northern Depression, Central Uplift, Southeast Uplift, Southeast Depression, Tangguzibasi Depression, and Southwest Depression (Fig. 1b; Jia, 1997). The Northern Depression can be further divided into four secondary tectonic units, including the Awati Depression, Shuntuoguole Low-Uplift, Manjiaer Depression, and Kongquehe Slope. The Central Uplift contains three secondary tectonic units, that is, the Bachu Uplift, Tazhong Uplift, and Guchengxu Uplift. In this

study, we also investigated the thermal evolution of the Kalpin Uplift in the northern margin of the Tarim Basin, which was part of the Tarim Block before the Cenozoic (Zhang et al., 2001; Chang et al., 2012a).

The Tarim Basin, with an Archean and Proterozoic crystalline basement, is overlain by a Paleozoic marine cratonic basin and a Mesozoic–Cenozoic foreland basin (Zhang, 2000; He et al., 2005; Zhang et al., 2013). The unified Tarim Craton formed during the Early Neoproterozoic (1.0–0.8 Ga) along with the collisions and the amalgamation of the North and South terranes, as was certified by zircon U-Pb data (Xu et al., 2013). According to research on the thick Neoproterozoic sedimentary succession, Zhu et al. (2017) and Wu et al. (2018) considered that the northern and southern Tarim Craton evolved as multiple rift basins were separated by the central paleo-uplift during the Late Neoproterozoic due to the breakup of the Rodinia supercontinent. The

Table 1

Measured zircon (U-Th)/He data from the Tarim Basin, Western China.

Grain No.	^{4}He (ncc)	Mass (mg)	F_T	U (ppm)	Th (ppm)	[eU] (ppm)	Corrected age + 1σ (Ma)	L (μm)	W (μm)	Rs (μm)
T1-04, Neoproterozoic volcaniclastic rock from the cutting samples at depth of 4660–4720 *m*										
z01	30.160	0.0079	0.81	234.7	120.9	263.1	117.9 ± 7.3	196.5	128.6	72.7
z02	21.286	0.0060	0.79	97.5	108.2	123.0	232.5 ± 14.4	176.5	120.6	67.4
z03	17.794	0.0101	0.78	19.0	25.7	25.1	549.0 ± 34.0	326.0	91.6	60.2
z04	20.502	0.0073	0.79	51.3	65.2	66.7	334.4 ± 20.7	233.5	99	61.3
z05	27.567	0.0046	0.75	167.0	149.5	202.1	237.3 ± 14.7	189.3	89.6	54.3
z06	100.473	0.0180	0.83	99.3	115.5	126.4	424.2 ± 22.9	265.0	121.6	74.2
z07	53.01	0.0163	0.83	67.1	70.2	83.6	377.0 ± 20.4	260.0	117	71.6
z08	77.868	0.0299	0.86	61.1	82.6	80.6	303.4 ± 16.3	289.5	150	89.4
z09	219.288	0.0459	0.89	62.8	79.8	81.6	524.2 ± 14.9	488.5	197.5	123.2
z10	145.281	0.0209	0.87	113.6	116.8	141.1	452.2 ± 13.1	241.5	189.5	102.1
z11	21.353	0.0057	0.79	94.4	89.3	115.4	333.9 ± 9.5	219	103.5	62.8
z12	23.853	0.0046	0.74	162.1	296.2	231.7	244.7 ± 6.5	212	77.5	49.1
BT5-12, Upper Devonian sandstone from the core samples at depth of 2514–2561 *m*										
z01	160.212	0.0120	0.81	755	575	890.3	152.0 ± 8.2	234.5	105.6	64.6
z02	147.233	0.0149	0.82	76	68	92.1	995.4 ± 55.2	236.5	117	70.3
z03	65.639	0.0112	0.81	127	97	149.3	389.7 ± 21.2	206.0	109	64.6
z04	173.040	0.0091	0.80	455.8	279.9	521.6	292.6 ± 18.1	250.9	106	65.6
z05	184.190	0.0095	0.81	421.9	117.6	449.5	343.8 ± 21.3	235.9	116	69.8
z06	133.454	0.0046	0.75	710.6	467.5	820.5	282.4 ± 17.5	183.5	92.4	55.4
z07	159.605	0.0134	0.84	236.8	207.6	285.6	333.4 ± 20.7	247.1	141.2	82.4
BT7-02, Middle Silurian sandstone from the core samples at depth of 5366.8 *m*										
z01	12.295	0.0014	0.65	660.2	405.8	755.6	94.4 ± 5.9	123.6	62	37.2
z02	27.987	0.0021	0.70	299.6	180.1	342.0	310.7 ± 19.3	149.2	67.2	41.1
z03	10.739	0.0013	0.64	292.6	42.1	302.5	222.6 ± 13.8	132.9	54.4	33.9
z04	22.508	0.0011	0.64	495.3	205.1	543.5	295.3 ± 18.3	108.1	61.8	36.0
WSL03, Ediacaran sandstone from the Kalpin outcrop										
z01	67.744	0.0048	0.76	183.5	191.6	228.5	648.5 ± 10.5	201	82	51.1
z02	19.107	0.0038	0.74	98.0	96.4	120.7	456.4 ± 7.5	195	73	46.1
z03	8.524	0.0008	0.59	575.1	1026.8	816.5	533.6 ± 9.2	111.5	46	28.6
z04	78.435	0.0618	0.89	14.9	24.7	20.7	551.4 ± 8.4	508	180.5	115.0
z05	277.109	0.0110	0.83	369.1	348.9	451.1	479.0 ± 7.6	279.5	128	78.1
z06	52.913	0.0267	0.87	29.4	37.9	38.3	700.2 ± 18.2	443.5	158	100.6
z07	12.159	0.0013	0.68	126.9	109.4	152.6	662.6 ± 11.6	132.5	64.5	38.9
z08	4.775	0.0008	0.63	89.2	91.7	110.7	648.5 ± 10.5	118	54	33.0
KQ1-03, Lower Silurian sandstone from the core samples at depth of 2600 ~ 3000 *m*										
z01	17.974	0.0079	0.78	34.1	98.0	57.2	408.9 ± 7.3	239	94.5	59.2
z02	29.501	0.0066	0.78	126.6	190.4	171.4	270.9 ± 5.1	226.5	92.5	57.6
z03	20.731	0.0046	0.77	74.3	49.4	85.9	547.5 ± 12.2	154	91	52.7
z04	33.210	0.0027	0.73	202.0	162.6	240.2	558.3 ± 13.2	124.5	81.5	46.1
z05	67.239	0.0040	0.76	241.2	203.5	289.0	604.7 ± 14.7	149.5	88.5	51.2
z06	22.184	0.0022	0.71	189.4	127.6	219.4	529.9 ± 12.9	122.5	71	41.3
z07	42.102	0.0041	0.75	203.0	127.5	232.9	477.3 ± 8.0	167.5	81	48.9
z08	24.207	0.0059	0.78	87.1	76.1	105.0	402.9 ± 6.6	178.5	97	57.2

Kalpin movement occurred during the end of the Late Ediacaran, and not only formed a disconformity between the Upper Ediacaran and Lower Cambrian (He et al., 2010; Yang et al., 2017; Chen et al., 2019) but also altered the tectonic paleogeomorphology, which played an important role in the formation and distribution of the Lower Cambrian Yuertusi source rock.

During the Early Cambrian, the entire Tarim Basin was inundated by seawater due to global transgression (Yang et al., 2011; Li et al., 2015a). The western and central Tarim Basin evolved as a cratonic carbonate platform and deposited thick dolomites, while the eastern Tarim Basin was in the deep-water shelf environment and dominantly deposited black shale, silicalite, mudstone, and marlstone (Li et al., 2015a; Chen et al., 2015). Along with the arid and tropical paleoclimate after the retreat of the sea, the Bachu Uplift, Tazhong Uplift, Awati Depression, and Shuntuoguole Low-Uplift evolved as an evaporating lagoon and deposited a set of gypsum and salt rocks with a maximum thickness of 400–450 m during the Middle Cambrian (Fig. 1b; Yang, 2015). The western and central Tarim Basin then developed as open, semi-restricted, and restricted platforms from east to west and deposited limestone and dolomites intercalated with reef and shoal deposits from the Late Cambrian to Middle Ordovician, while the eastern Tarim Basin evolved as basin-slope facies and deposited limestone and argillaceous limestone. The entire Tarim Basin developed in a deep-sea environment during the Late Ordovician and deposited siliciclastic formations (Lin

et al. 2012). During the Silurian, the central Tarim Basin evolved as a coastal, shallow sea and dominantly deposited mudstones and sandstones, while the northern and southern Tarim Basin continuously experienced erosion (Zhang et al., 2008; Chang et al., 2012b). Due to the stress transition from extension to compression, most of the Tarim Basin experienced uplifting and erosion from the end of the Silurian to Middle Devonian (Guo and Hong, 2007). Due to the transgression at the end of the Late Devonian, the notable Donghetang sandstone sequence, characterized by upper pebbly sandstone, middle pure sandstone, and bottom conglomerates, deposited on the top of the Upper Devonian in the Tarim Basin (Zhang et al., 2004). The Tarim Basin remained in an epicontinental marine environment during the Carboniferous and mainly deposited littoral and neritic clastic sediments. During the Early Permian, a large igneous province formed with dramatic magmatic activity in the northwestern Tarim Basin (Li et al. 2011, 2012; Xu et al., 2014). During the Late Permian, the Tarim Basin evolved from a marine basin into a fluvial and lacustrine intercontinental basin together with the closure of the South Tian Shan Ocean. Since the Mesozoic, the northern and southwestern margins of the Tarim Basin developed as a foreland basin. Several kilometers of clastic rocks, including conglomerates, sandstones, and mudstones, were deposited in the Kuqa Depression, Kashi Depression, and Southwestern Depression (Chang et al., 2017). Due to the complex tectonic and sedimentary evolution histories, many disconformities or angular unconformities formed in the
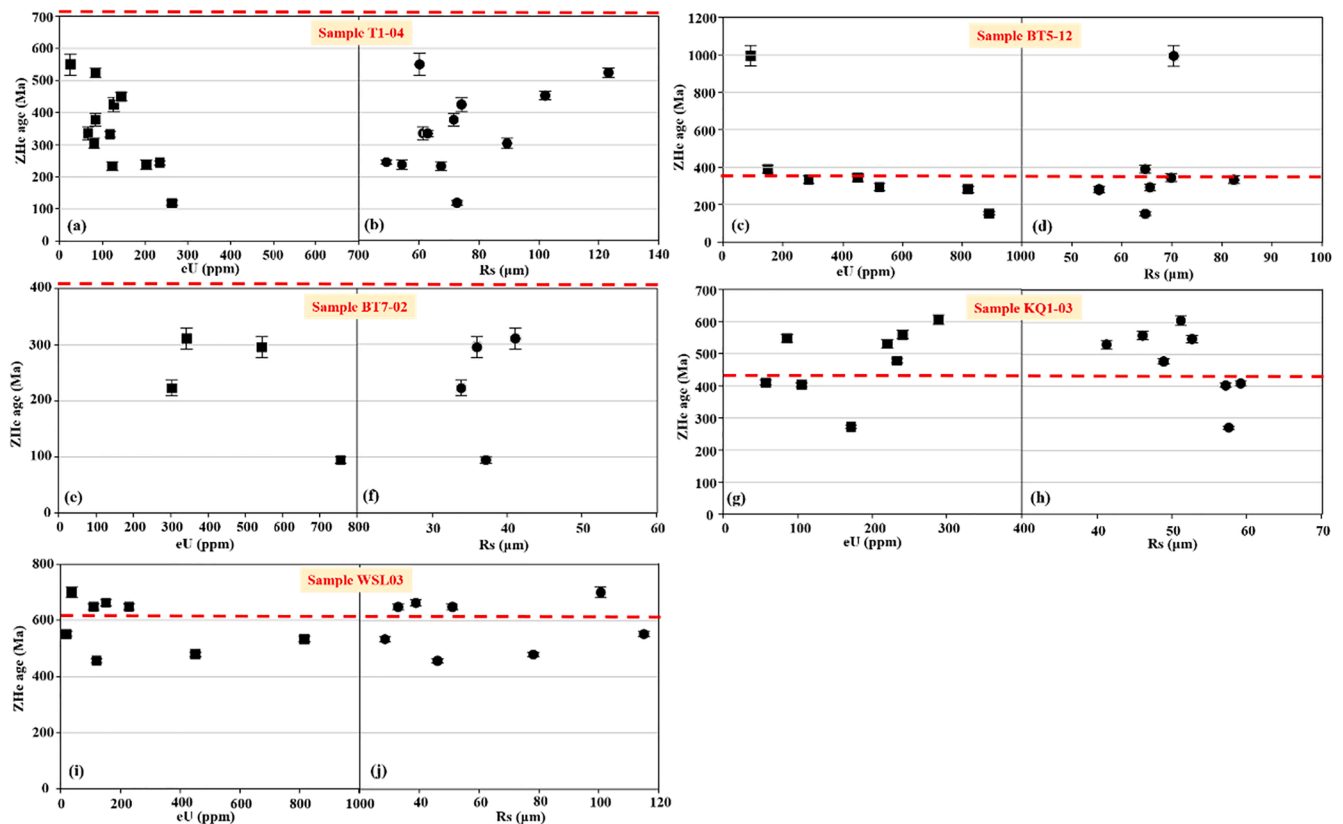
Fig. 3. the correlation of single-grain ZHe ages with eU content and Rs for the studied samples. The red dashed lines represent the depositional ages of the samples. Because the depositional age of the samples T1-04 and BT7-02 is beyond the Y-axis maximum age, the red dashed lines is outside the rectangles. (For interpretation of the references to colour in this figure legend, the reader is referred to the web version of this article.)

Tarim Basin (Fig. 1c, 1d and 2).

3. Zircon (U–Th)/He (ZHe) methods, sampling, and results

Zircon (U-Th)/He thermochronology is based on the accumulation of alpha particles (^{4}He) produced by the radioactive decay of the parent isotopes U and Th. The Radiogenic ^{4}He can be lost by diffusion to the mineral margin, which occurs as a function of temperature. Thus, the concentrations of ^{4}He and the parent isotopes can be used to calculate a zircon (U-Th)/He age, which represents a cooling event one rock experienced. Generally, the rocks with the zircon (U-Th)/He ages, younger than the depositional ages, are suitable for studying the thermal history of the basins with thermal modeling. Except for the temperature, the retentivity of He diffusivity in zircon crystals is also influenced by the damage in the crystal lattice due to self-irradiation. The degree of damage in zircon can be quantified by its alpha dose, which represents the number of alpha decay events per gram of zircon. Guenthner et al. (2013) suggested that increasing amounts of damage initially decrease He diffusivity in zircon, but after accumulated damage exceeds a critical threshold (~2×10^{18} α/g), He diffusivity increases with further damage. The positive correlations between ZHe age and eU (effective uranium concentration, eU = U + 0.235 Th) represent the effects of increasing radiation damage on helium diffusion at low alpha doses, whereas negative age-eU correlations are indicative of grains with moderate to high α doses, which experienced a protracted thermal history at temperatures cooler than the ZFT partial annealing zone (Guenthner et al., 2013, 2017; Powell et al., 2016). When the detrital samples just experienced partial resetting after deposition, some zircon grains probably inherited some radiation damage and He concentration generated in the source region (Guenthner et al., 2015), which can result in a more complicated correlation between the single-grain ZHe ages and eU

contents.

In this study, five samples T1-04, BT5-12, BT7-02, KQ1-03, and WSL03 were collected for studying the thermal evolution of the Tarim Basin. Sample T1-04, collected at the depths of 4660–4720 m of Well T1 in the northwestern corner of the Bachu Uplift (Fig. 1b), is a Cryogenian volcaniclastic rock with its youngest zircon U-Pb age being ∼ 707 ± 8 Ma (Yang et al., 2017). The Upper Devonian sandstone sample BT5-12 was obtained from the depths of 2514–2561 m of Well BT5 in the western margin of the Bachu Uplift (Fig. 1b), while the Middle Silurian sandstone sample BT7-02 was collected from Well BT7 at a depth of 5388.6 m in the northeastern margin of the Southwest Depression. The Lower Silurian sandstone sample KQ1-03 was collected at depths of 2600–3000 m of Well KQ1 in the southern Kongquehe Slope. The only outcrop sample, WSL03, collected from the Kalpin Uplift, belongs to the Ediacaran sandstone with its youngest zircon U-Pb age being 602 ± 16 Ma (Li et al., 2015b). The zircon grains for each sample were separated using conventional heavy liquid and magnetic separation techniques. The measurement of ZHe ages was performed at the low-temperature thermochronology laboratories of the University of Melbourne, the University of Arizona, and the University of Florida, and the detailed experimental procedures were introduced in the supporting information and can also refer to Gleadow et al. (2015), Reiners and Stefan (2006), and Chang et al. (2019), respectively. The samples' information and measured ZHe data are shown in Table 1. Note that some single-grain ZHe data for samples T1-04, WSL03, and KQ1-03 were reported in previous studies by Chang et al. (2011) and Qiu et al. (2012).

The single-grain ZHe ages of each sample exhibit obvious dispersion (Fig. 3), implying a potentially complex, protracted thermal history. Except for sample KQ1-03, the oldest individual ZHe ages for the remaining samples usually correspond to relatively low eU content. The twelve single-grain ZHe ages of sample T1-04, younger than the
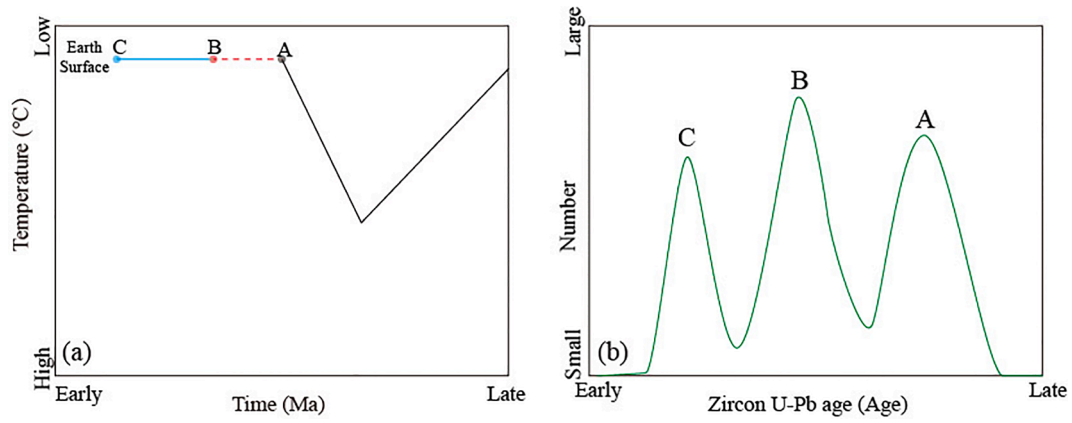
Fig. 4. (a) Schematic diagram for the starting time of forward thermal modeling. (b) Schematic diagram of the zircon U-Pb peak ages for one sample.

depositional age, are broadly distributed between 549 ± 34.0 Ma and 117.9 ± 7.3 Ma and show an obvious negative correlation with the eU contents. The majority of the single-grain ZHe ages for sample BT5-12 (5 out of 7 total grains) are younger than the depositional age, except for two grains with ZHe ages of 995.4 ± 55.2 Ma and 389.7 ± 21.2 Ma, exhibiting very low eU content with 92.1 ppm and 149.3 ppm,
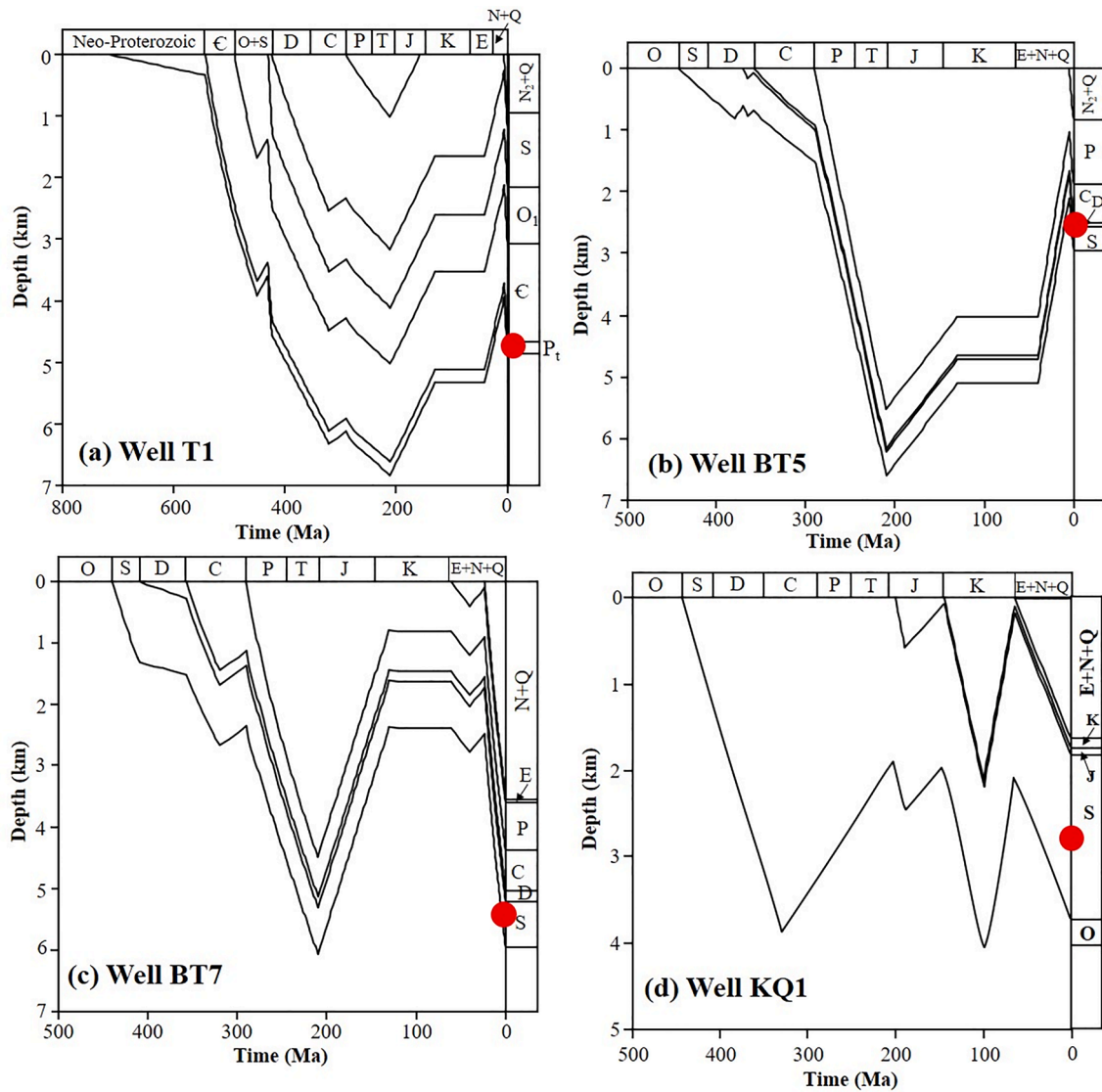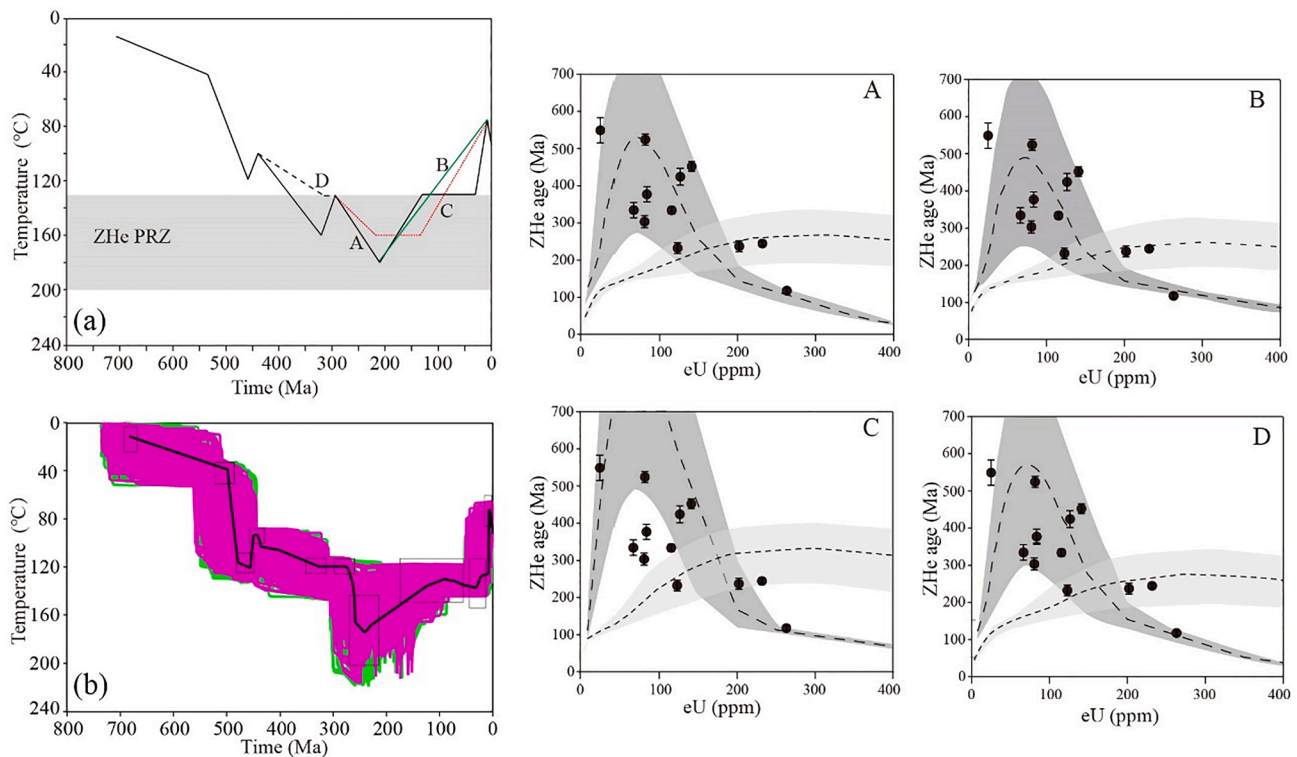

Fig. 5. Reconstructed burial histories of the wells T1, BT5, BT7 and KQ1, showing the remaining strata, the uplift events (gotten from the thermal histories in this study) and the samples' location with red circles. (For interpretation of the references to colour in this figure legend, the reader is referred to the web version of this article.)

Fig. 6. Forward (a) and inverse (b) thermal history of the sample T1-04 (Chang et al., 2022). The forward modeling provided four specific t-T paths A, B, C and D, generating the right inheritance envelopes A, B, C and D, respectively. All the envelopes (Dark gray = 2000 Ma, light gray = 710 Ma) correspond to date-eU trends for zircon between 53 μm (lower bond) and 95 μm (upper bond) Rs. The dashed line in each inheritance envelope represents the date-eU trend for the zircons with 74 μm (mean Rs). For the inverse model (b), black boxes indicate t-T constraints and the solid black line represents the best fitting thermal path. Good paths are represented by the magenta lines, whereas acceptable paths are represented by green lines. ZHePRZ represents the zircon helium partial retention zone with a temperature range of 130–200 °C (Wolfe and Stockli, 2010). (For interpretation of the references to colour in this figure legend, the reader is referred to the web version of this article.)

respectively. Four single-grain ZHe ages of sample BT7-02 range from 94.4 ± 5.9 Ma to 310.7 ± 19.3 Ma, younger than the depositional age, indicating an obvious negative correlation with the eU contents. The negative correlation between the single-grain ZHe ages and eU for the samples T1-04, BT5-12, and BT7-02 indicates the differential partial resetting caused by the radiation damage. For sample KQ1-03, the measured eight single-grain ZHe ages are intricately distributed between 270.9 ± 5.1 Ma and 604.7 ± 14.7 Ma, and there are only three single-grain ZHe ages younger than the depositional age. For the sample WSL03, only four single-grain ZHe ages of 456.4 ± 7.5 Ma, 533.6 ± 9.2 Ma, 551.4 ± 8.4 Ma, and 479.0 ± 7.6 Ma are younger than the depositional age, and its complicated correlation between the single-grain ZHe ages and eU contents is shown in Fig. 3i and 3j. Besides, there is no correlation between the single-grain ZHe ages and Rs for most samples (Fig. 3), except for sample KQ1-03, which indicates a slightly negative correlation.

4. Thermal modeling

The obvious dispersion of single-grain ZHe ages for each rock may have been influenced by inherited radiation damage and residual He before deposition (Fig. 3). Traditional data processing methods, including calculating the weighted mean ZHe age by averaging single-grain dates or discarding older or younger ages outside the expected date range, would result in the removal of the useful and pertinent information on burial temperatures and cooling rates for the studied samples (Powell et al., 2016). The ZRDAAM kinetic model and inheritance envelope concept, successively proposed by Guenthner et al. (2013, 2015), provides the opportunity to study the protracted thermal histories of rocks with intricate single-grain ZHe ages. The inheritance envelope concept is a useful means of addressing plausible post-

depositional temperature–time (t-T) hypotheses for all ZHe data sets from rocks with variable pre-depositional histories. If the inheritance envelope generated by a specific t-T path and a reasonable range of possible pre-depositional inheritance ages encompasses the full range of a sample's date variability, then the corresponding path is a plausible solution to explain the rock's thermal history (Guenthner et al., 2015).

In this study, first, the HeFTy thermal modeling software developed by Ketcham (2005) was used to run forward modeling for the given t-T paths of each sample with specific radius and eU contents in terms of the ZRDAAM kinetic model of Guenthner et al. (2013). Then, the simulated ZHe ages and relevant specific eU contents were plotted for acquiring the inheritance envelope of each t-T path. Finally, we projected the measured ZHe ages and eU contents onto the inheritance envelope to determine each optimal t-T path. The path was considered optimal if most single-grain ages could fall into the inheritance envelope of a specific t-T path. The given t-T paths for each sample were found to be dependent on the local formation thickness, the occurrence of unconformities, and regional tectonic evolution. Two consensuses of the thermal modeling were that the heating for each sample was consistent with burial since deposition and the timing and magnitude of cooling were related to exhumation. Considering the inherent radiation damage and the complexity of provenance, the starting times (given in Ma) of each t-T path for forward modeling were set according to the depositional time and zircon U-Pb peak ages for the studied samples (Fig. 4). The point A represents the depositional time for the zero-inheritance zircon He ages, which usually equal to the youngest zircon U-Pb peak age. The point B and C, equal to two older zircon U-Pb peak ages, were as the starting times for the inheritance zircon He ages. The paleo-surface temperature when the samples deposited in the Tarim Basin was set to be ∼ 14 °C. For the drilling samples, the present-day burial temperatures of the drilling samples are calculated based on the surface temperature,
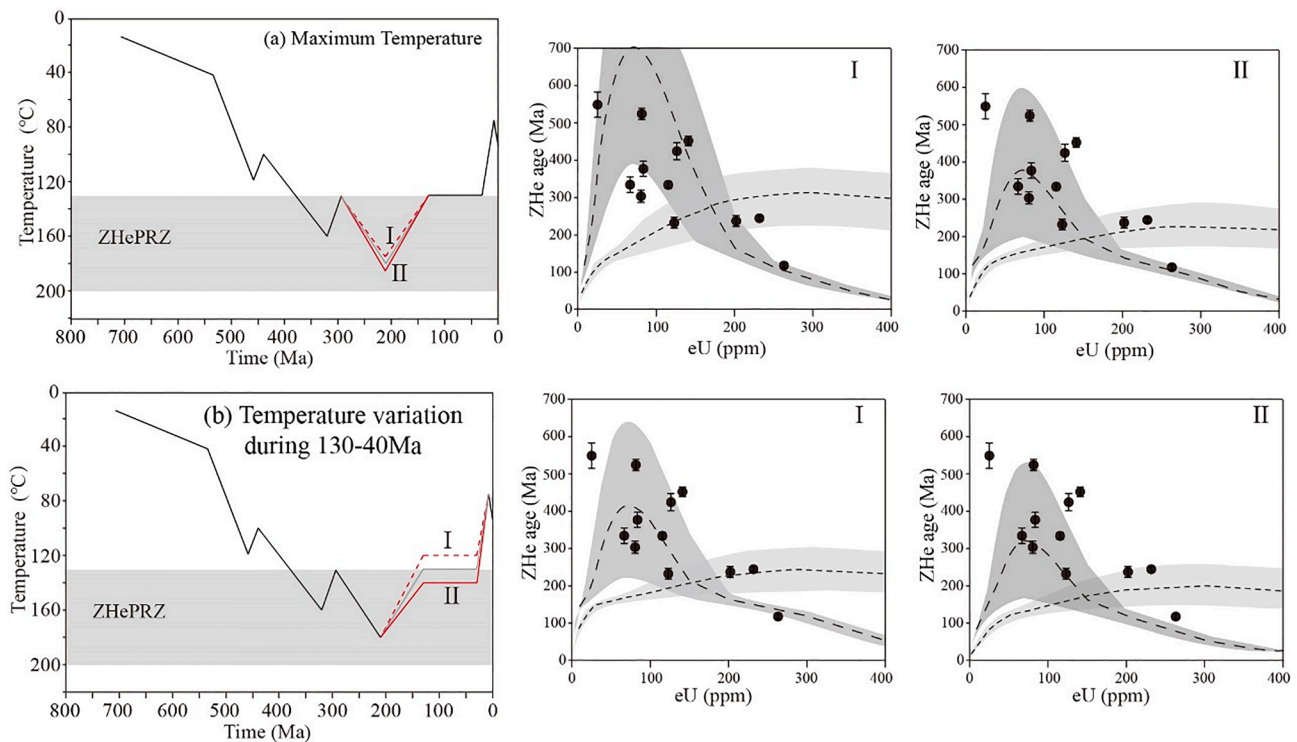
Fig. 7. t-T paths and corresponding inheritance envelopes for the sample T-04 (Chang et al., 2022). In (a) and (b), the solid gray t-T paths are fixed and correspond to the pattern A in Fig. 6a. The dashed and solid red T-t curves (I, II) exhibit the effect of changing a) maximum temperature (±5 °C) in 210 Ma and b) the temperature during 130–40 Ma (±10 °C). To the right, the corresponding date-eU inheritance envelopes for the grain size between 53 μm (lower bond) and 95 μm (upper bond) are shown with the dark (2000 Ma) and light (710 Ma) gray areas, in which the dashed blacks lines corresponding to the mean radius of 74 μm were plotted. ZHePRZ represents the zircon helium partial retention zone with a temperature range of 130–200 °C (Wolfe and Stockli, 2010). (For interpretation of the references to colour in this figure legend, the reader is referred to the web version of this article.)

geothermal gradient and burial depth of the samples (Fig. 5; Liu et al., 2016). The residual strata of the wells T1, BT5, BT7 and KQ1 and their contact relationship were shown by the burial histories (Fig. 5), which also indicate the time and amplitude of the tectonic uplift events gotten from the thermal modeling of the samples as mentioned below. The erosion thickness for each tectonic uplift event is equal to the temperature reduction in the thermal histories (this study) divided by the paleo-geothermal gradient (Qiu et al., 2012). In addition, inverse thermal modeling for samples T1-04, BT5-12, and BT7-02 was carried out to assess the plausible t-T histories obtained from the forward modeling, while those of the samples WSL03 and KQ1-03 refer to the studies by Chang et al. (2011) and Qiu et al. (2012), respectively.

4.1. Cryogenian sample T1-04, Bachu Uplift

It should be noted that Neo-Proterozoic, Cambrian, Lower Ordovician, Lower-Middle Silurian, Pliocene, and Quaternary are present in the Well T1 area (Fig. 5a), indicating that this area experienced multi-stage tectonic movements. According to the configuration of unconformities as well as previous research on the tectonic evolution of the Bachu Uplift and adjacent regions (Chang et al., 2012a, 2014, 2019), the exhumation (cooling) or hiatus events at the end of the Ordovician, Late Carboniferous, Jurassic, Cretaceous, and Paleogene-Miocene were set for forward modeling of sample T1-04 (Fig. 6a). Meanwhile, the 2000 Ma (inheritance) and 710 Ma (zero-inheritance, as the depositional age), obtained from zircon U-Pb peak ages (Yang et al., 2017), were set as the starting times for forward modeling. Four patterns of t-T paths A, B, C, and D were given for assessing the differences between the measured single-grain ZHe ages and inheritance envelopes (Fig. 6a). Patterns A and D with a maximum temperature of ~ 180 °C in ~ 210 Ma generated similar good fits for the inheritance envelopes and single-grain ZHe ages,

with the exception of the oldest ZHe age, implying that subtle temperature variation for the t-T path other than the maximum temperature point does not affect the inheritance envelopes. According to seismic data, Zheng (2016) concluded that the northwestern Bachu Uplift (including Well T1) experienced tectonic uplift at the end of the Carboniferous, which eroded all of the Upper Carboniferous strata. This cooling event was probably related to the collision of the Tarim block with the Central Tian Shan during the Late Carboniferous to Early Permian (Han et al., 2011; Yang et al., 2012). Therefore, as the best t-T path, pattern A is strongly in accordance with the actual tectonic evolution in the Bachu Uplift. Meanwhile, an inversion result similar to pattern A was also obtained by the measured ZHe ages (Fig. 6b). For pattern B, one rapid cooling event was set for a time interval of 210–40 Ma, which is different from that in pattern A. First, pattern B is not consistent with the actual tectonic evolution in the Bachu Uplift. Previous studies suggested that most of Central Asia stayed in tectonic quiescence and formed paleo-planation surfaces from Late Jurassic to Paleogene after the Early–Middle Jurassic rapid uplift (Jolivet et al., 2015; Morin et al., 2019), which was also revealed by the explanation of thermal history of the Kalpin Uplift (Chang et al., 2019). Therefore, the Well T1 area near the Kalpin Uplift is likely to have experienced similar tectonic evolution from the Early Jurassic to Neogene (Chang et al., 2019). Second, three single-grain ZHe ages do not fall into the inheritance envelopes compared to patterns A and D. Pattern C is also significantly different from pattern A. It is assumed that there was a tectonic quiescence from 210 to 130 Ma with a maximum temperature of 160 °C and subsequent rapid cooling from 130 Ma. There are four single-grain ZHe ages not to fall into the inheritance envelopes. Therefore, the Pattern C is not in accordance with the actual geological setting. In addition, we attempted to modify the temperature at 210 Ma and from 130 Ma to 40 Ma to assess the fitting of the ZHe ages and
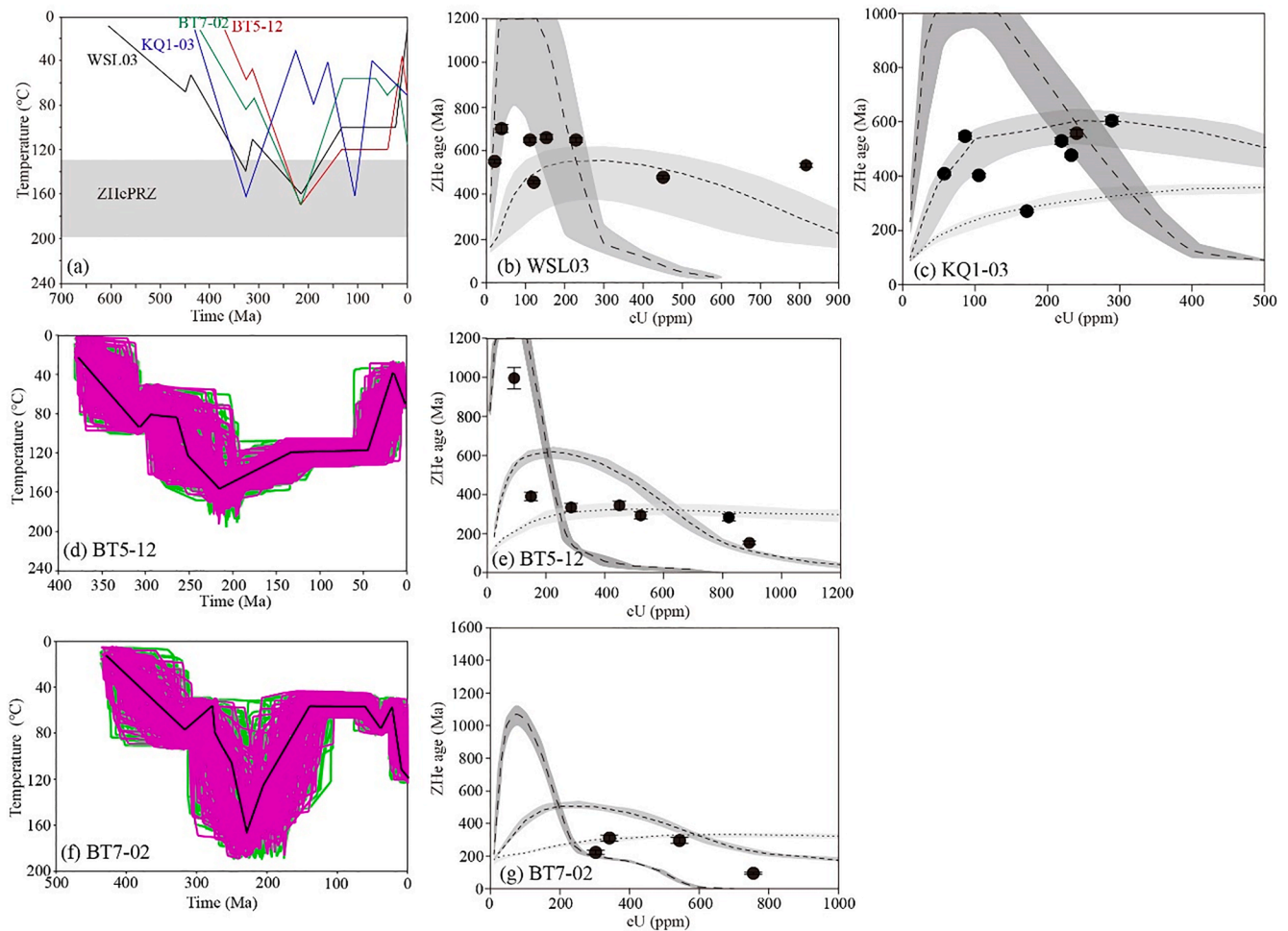
Fig. 8. (a) Specific t-T paths for forward modeling of the samples WSL03, KQ1-03, BT5-12 and BT7-02; (b), (c) (e) and (g) Inheritance envelopes for the samples WSL03, KQ1-03, BT5-12 and BT7-02, respectively. For sample WSL03, Dark gray = 1900 Ma, light gray = 750 Ma, the dashed line represents the date-eU trend with the mean radius of 61 μm, the lower and upper bonds for the envelopes correspond to the radii of 28 μm and 94 μm, respectively; For sample KQ1-03, Dark gray = 1500 Ma, Middle gray = 800 Ma, light gray = 440 Ma, the dashed line represents the date-eU trend with the mean radius of 52 μm, the lower and upper bonds for the envelopes correspond to the radii of 46 μm and 58 μm, respectively; For sample BT5-12, Dark gray = 1950 Ma, Middle gray = 850 Ma, light gray = 450 Ma, the dashed line represents the date-eU trend with the mean radius of 68 μm, the lower and upper bonds for the envelopes correspond to the radii of 59 μm and 76 μm, respectively. For sample BT7-02, Dark gray = 1800 Ma, Middle gray = 800 Ma, light gray = 430 Ma, the dashed lien represents the date-eU trend with the mean radius of 37 μm, the lower and upper bonds for the envelopes correspond to the radii of 34 μm and 40 μm, respectively. (d) and (f) the inverse thermal histories of the samples BT5-12 and BT7-02, respectively. The solid black line represents the best fitting thermal path. Good paths are represented by the magenta lines, whereas acceptable paths are represented by green lines. ZHePRZ represents the zircon helium partial retention zone with a temperature range of 130–200 °C (Wolfe and Stockli, 2010). (For interpretation of the references to colour in this figure legend, the reader is referred to the web version of this article.)

inheritance envelopes (Fig. 7). When the maximum temperature at 210 Ma was set to 175 °C and 185 °C, there are two single-grain ZHe ages not to fall into the inheritance envelopes (Fig. 7a). When the temperatures from 130 Ma to 40 Ma was set to 120 °C and 140 °C, three and five single-grain ZHe ages did not fall into the inheritance envelopes, respectively (Fig. 7b). These modeling results also indicates that the pattern A is the best thermal path for the sample T1-04.

4.2. Upper Devonian sample BT5-12, Bachu Uplift

Upper Devonian, Carboniferous, Permian, Pliocene, and Quaternary deposits are found above sample BT5-12 in the Well BT5 area (Fig. 5b). Owing to the close distance between wells BT5 and T1, we give a t-T path after the deposition, similar to sample T1-04, for the forward modeling of sample BT5-12 (Fig. 8a). According to the zircon U-Pb peak ages (Guo et al., 2017), three ages of 1950 Ma, 850 Ma, and 450 Ma were set as the starting times for forward modeling to assess the effectiveness of the inheritance envelopes. As the best t-T path, the maximum formation temperature at 210 Ma was set at 170 °C, and accordingly, five

single-grain ZHe ages fell into the envelopes (Fig. 8e). In addition, the inversion result shows a similar t-T path (Fig. 8d).

4.3. Middle Silurian sample BT7-02, Southwest Depression

Middle-Upper Silurian, Devonian, Carboniferous, Lower-Middle Permian, Upper Paleogene-Eocene, Neogene, and Quaternary deposits are found above sample BT7-02 in the Well BT7 area (Fig. 5c). Previous studies confirmed that the eastern margin of the Southwest Depression (including Well BT7 area) experienced a similar tectonic evolution with the Bachu Uplift before the Cenozoic (Sobel, 1999; Zheng, 2016); therefore, we designed a specific t-T path similar to that of sample T1-04 from the Middle Silurian to Early Paleogene (Fig. 8a). The Paleogene transgression of the NeoTethys Ocean occurred in the western part of the Tarim Basin, leading the Well BT7 area to become inundated by seawater and receive deposition during the Late Paleogene-Eocene (60–40 Ma) (Shao et al., 2006; Bosboom et al., 2014; Sun et al., 2016a). During the Late Eocene, the northward indentation of the Pamir in response to the ongoing India-Asia collision not only resulted in sea

retreat but also caused the Bachu Uplift and western margin of the Southwest Depression (including the Well BT7 area) to undergo uplift and erosion with SW-NE compression (Buslov et al., 2003; Carrapa et al., 2015; Sun et al., 2016b, 2020). Since the Early Miocene (20 Ma), the area of Well BT7 has become the western margin of the Southwest foreland basin due to the reactivation of the Selibuya fault zone and has accumulated sediments with a thickness of ~3000 m (Zheng et al., 2016; Zhang et al., 2019). According to the tectonic evolution mentioned above, the specific t-T path with three possible starting times of 1800 Ma, 800 Ma, and 430 Ma was given for the forward modeling of sample BT7-02 (Chang et al., 2012b; Fig. 8a). For the best t-T path with a maximum temperature of 170 °C at 210 Ma, three single-grain ZHe ages fall in the envelopes with the exception of 94.4 ± 5.9 Ma (Fig. 8g). The inversion thermal history further indicated that the best t-T path was valid (Fig. 8f).

4.4. Ediacaran sample WSL03, Kalpin Uplift

The inversion thermal histories of sample WSL03, obtained from the combination of zircon and apatite (U-Th)/He data (Chang et al., 2011), suggest that the Ediacaran strata reached a maximum temperature range of 140 °C to 160 °C in the Early Carboniferous and Early Jurassic. To further understand the t-T conditions capable of constraining all the single-grain ZHe ages, we extracted a t-T path from the inversion results to run forward modeling with starting times of ~ 1900 Ma and 750 Ma to assess the effects of changing the maximum temperature on date-eU relationships (Li et al., 2015b) (Fig. 8a and 8b). As the best t-T path, with the maximum temperature at 210 Ma set to 160 ℃, most ZHe ages fell into the inheritance envelopes. It is inferred that the excessive F_T correction induces a ZHe age of 533.6 ± 9.2 Ma out of the envelopes because this grain has a radius of just ~ 28.6 μm, which is smaller than the proposed value (~30 μm) (Farley et al., 1996).

4.5. Lower Silurian sample KQ1-03 and Kongquehe Slope

Fig. 5d shows the burial history of Well KQ1, showing the residual strata and uplifting events. Qiu et al. (2012) reported the inversion thermal history of sample KQ1-03 based on the apatite fission track (AFT), apatite (U-Th)/He (AHe), and ZHe ages. In this study, we evaluate the effects of changing the maximum temperature on date-eU relationships by extracting a specific t-T path for forward modeling from the inverse modeling (Fig. 8a and 8c). Three starting times of 1500 Ma, 800 Ma, and 440 Ma were set for forward modeling (Chang et al., 2012b). The best t-T path indicated that when the maximum temperature during the Early Devonian and Early Cretaceous was set to 160 ℃, all the single-grain ZHe ages could fall into the age-eU envelopes. It should be noted that the highest temperature during the Early Devonian by the inversion result was only 140–150 °C, which was lower than that of the forward modeling.

5. Discussion

### 5.1. Effectivity of forward modeling with zircon (U-Th)/He data

Distinguished from previous studies (Orme et al., 2016; Guenthner et al., 2017; Delucia et al., 2018), this study first carried out an analysis of the thermal histories of the drilling samples from the Tarim Basin by forward modeling with the ZRDMM model. It should be noted that the latter heating with burial and the current high temperature is likely to have partly affected the radiation damage and helium preservation, resulting in the complexity of single-grain ZHe age distribution. To reduce this complexity, only samples with current formation temperatures lower than 130 °C were collected. The forward modeling of single-grain ZHe ages revealed the burial highest temperature of sample BT5-12 in the Early Jurassic, consistent with that recorded by the R_{equ} data. However, the burial highest temperatures of the WSL03 and KQ1-

03 obtained from the forward modeling were slightly higher than the inversion results (Chang et al., 2011; Qiu et al., 2012). Several recent studies have acknowledged that the ZRDAAM model has not been successfully applied to zircons with a relatively high radiation damage dose (Powell et al., 2016; Anderson et al., 2017; Johnson et al., 2017; Green et al., 2018). Green et al. (2018) considered that the t-T path obtained by the ZRDAAM model, which can reproduce measured ZHe data, requires a relatively long period of residence at low temperatures (<200 °C). The ZRDAAM model proposed by Guenthner et al. (2013) utilizes etchable fission track annealing as a proxy for bulk radiation damage annealing. The radiation damage in zircon is composed of recoil tracks, point defects, and interstitial helium with different repair kinetics (Geisler and Pidgeon, 2002; Jonkheere et al., 2019). Therefore, the ZRDAAM model always underestimates the radiation damage dose and produces more biased thermal histories for zircons with higher radiation damage doses. In addition, eU and radiation damage zoning also play an important role in the thermal modeling of zircon (U-Th)/He data (Guenthner et al., 2015; Anderson et al., 2017). Although the inheritance envelopes with different staring times could explain the measured ZHe data, it was difficult to make a one-to-one correspondence for the single-grain ZHe data and zircon U-Pb age. To obtain more effective thermal information for the detrital samples by the ZRDAAM model, the zircon U–Pb, ZHe, and radiation damage zoning (or eU zoning) for one zircon should be measured in the future.

5.2. The relationship between the cooling events and the tectonic uplifting events

Our data and thermal modeling suggest that the Tarim Basin experienced multiple thermal histories during the Phanerozoic. The Late Ordovician cooling events revealed by the samples from the Bachu Uplift and the Kalpin Uplift was related to the closure of the Proto-Tethys Ocean (Zhang et al., 2017; Li et al., 2018; Wu et al., 2020, 2021). This tectonic event also caused the Kongquehe Slope in eastern Tarim Basin to experience intense erosion and formed an unconformity between Middle Ordovician and Lower Silurian (Qiu et al., 2012). Previous studies indicated that some transpressional strike-slip faults and karst landform, which play an important role in hydrocarbon migration and accumulation, developed in the central Tarim Basin and Tabei Uplift due to the late Ordovician tectonic activity (Zhang et al., 2010; Qiu et al., 2019; Deng et al., 2019), respectively. The Late Carboniferous cooling events in the Bachu Uplift, Kalpin Uplift and Kongquehe Slope resulted from the closure of the South Tianshan Ocean (Han et al., 2011; Ge et al., 2014; Han and Zhao, 2018; Alexeiev et al., 2019; Wu et al., 2020), which also led to the formation of massive magmatic rocks with the zircon U-Pb ages of 315 ~ 270 Ma (Han et al., 2011; Han and Zhao, 2018). During the Late Triassic, the Qiangtang terrane collided with the southern margin of the Asian continent (Yin and Harrison, 2000), causing that the Northern Kunlun terrane (the present Western Kunlun) to be thrust rapidly onto the southwest margin of the Tarim basin (Yin and Harrison, 2000; Robinson et al., 2004). The Southwest Depression developed as the foredeep part of a foreland basin and accommodated several kilometers of fluvial and lacustrine sediments (Sobel, 1999). The Bachu Uplift and Kalpin Uplift probably evolved into the forebulge part of the foreland, and began to be eroded seriously, which was recorded by the thermal histories, AFT, and ZFT ages (This study; Dumitru et al., 2001; Chang et al., 2014). The comprehensive analysis on the low-T thermochronological data suggests that most of Central Asia developed under a paleo-planation surface from the Late Jurassic to early Cenozoic and underwent a protracted period of extremely slow cooling (Jolivet et al., 2015). This is confirmed by the widespread preservation of large fragments of the paleo-planation surfaces within the Tian Shan range (Morin et al., 2019). This is also consistent with our thermal modeling results. The reactivation of the Kepingtag Fault in the southern margin of the Kalpin Uplift and the Selibuya Fault in the western margin of the Bachu Uplift finally resulted in the differential tectonic uplift or subsidence
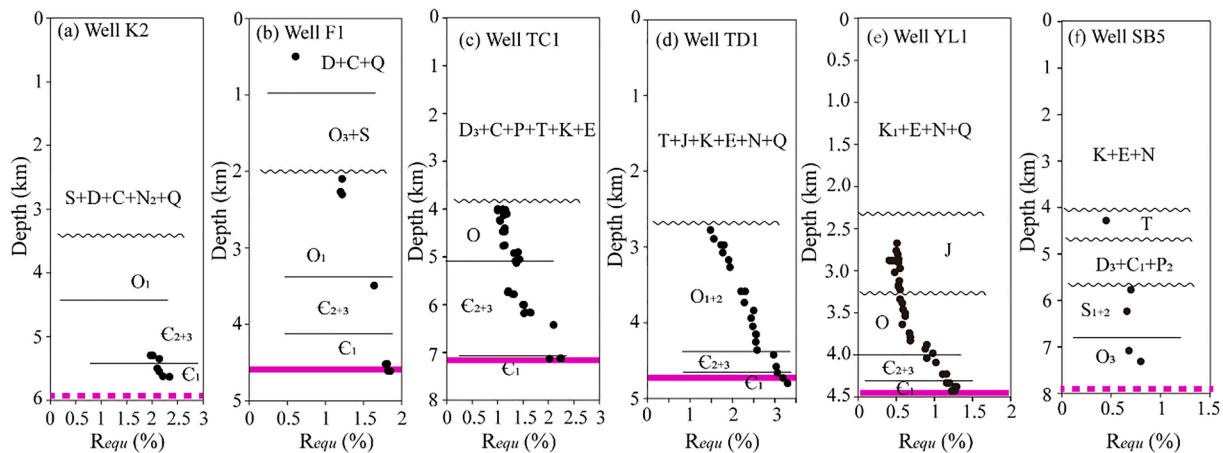
Fig. 9. Correlation of the equivalent vitrinite reflectance (Requ) with the wells' depths. The solid magenta lines represent the drilled depths of the Yuertusi source rock, the dashed magenta lines represent the inferred depths of the Yuertusi source rock. (For interpretation of the references to colour in this figure legend, the reader is referred to the web version of this article.)
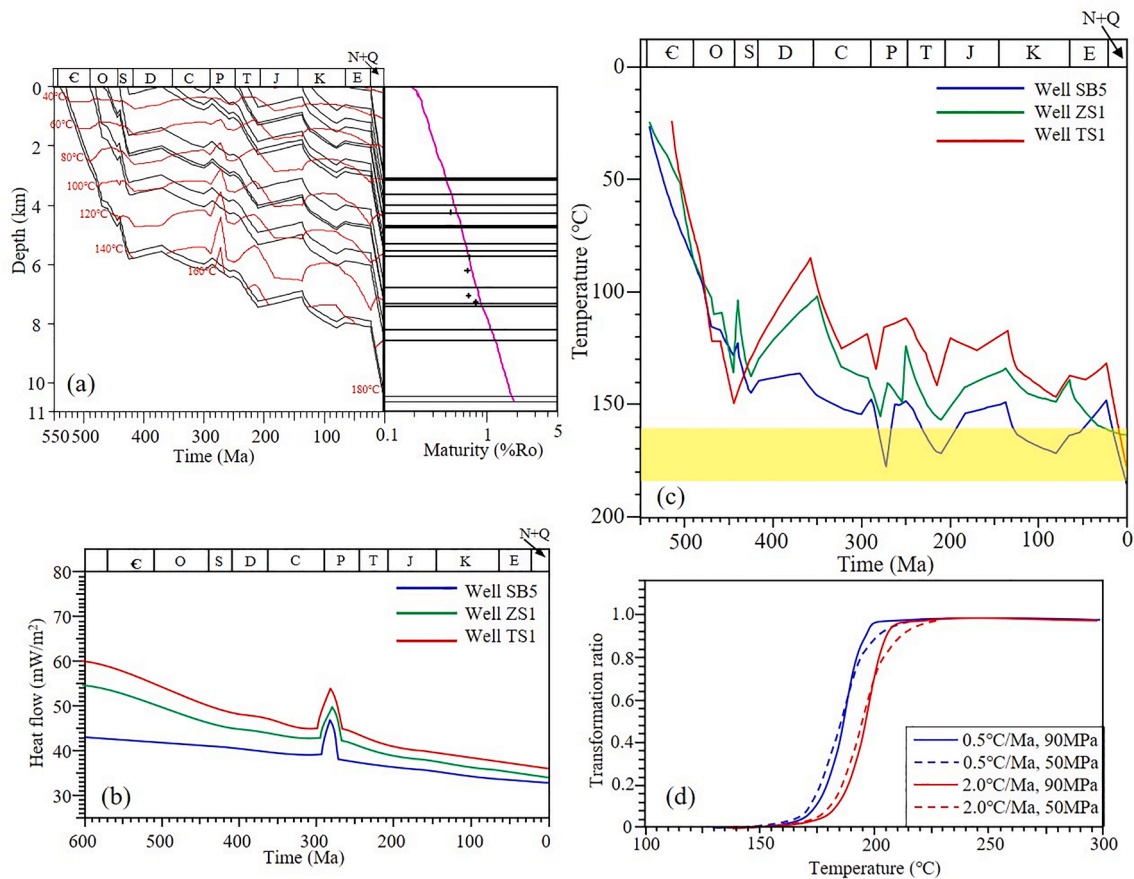
Fig. 10. (a) Buried and temperature history of the Well SB5 (left) and the correlation of the measured Ro data (+) and simulated result with pink lines (right); (b) The paleo-heat flow evolution history of the Wells SB5, ZS1 and TS1 (Li et al., 2010, 2022); (c) Temperature histories of the bottom of the Cambrian for the Wells SB5 and ZS1 and the bottom of the Upper Cambrian for the Well TS1 according to the buried and heat flow history; (d) Cracking transformation ratio of the crude oil from the Ordovician reservoir in the Shunbei area at different pressures and heating rates (Li et al., 2021). (For interpretation of the references to colour in this figure legend, the reader is referred to the web version of this article.)

among the Kalpin Uplift, Bachu Uplift, and Southwest Depression since the Miocene (Zheng et al., 2016; Chang et al., 2012a, 2019; Zhang et al., 2019). The Late Cretaceous cooling events in the Kongquehe Slope in the eastern Tarim Basin was considered to be related to the collision of the Dras–Kohistan arc and the southern margin of Eurasia plate (Zhang et al., 2011; Glorie et al., 2011; Clift et al., 2014).

5.3. Thermal effect on the deep source rocks and reservoirs in the Tarim Basin

According to the high total organic carbon (TOC) content, the Lower Cambrian Yuertusi Formation and Middle Ordovician Saergan Formation are considered to be superior source rocks (Yun et al., 2014). In this

study, the vitrinite-like maceral reflectance (R_v) and bitumen reflectance (R_b) from the Cambrian and Ordovician strata of seven wells K2, F1, TC1, TD1, YL1, XH1, and SB5 were collected and converted into the equivalent vitrinite reflectance values (R_{equ}) using the formulae of Jacob (1989), Liu and Shi (1994), and Xiao et al. (2000) (Fig. 9). According to the paleo-geothermal gradient of 24.8 °C /km (Chang et al., 2016) and depth differences, the experienced highest temperature of the formation at the depth of ~ 5290 m in Well BT5 was calculated to be ~ 237.9 ℃, almost equivalent to that of the nearby well K2 (240.8–243.4 ℃), further indicating that the forward modeling with the single-grain ZHe ages is valid. The Lower Cambrian R_{equ} data of wells K2, F1, TC1, and TD1 are larger than 2%, implying that the Yuertusi Formation source rock in the Central Uplift (including Bachu Uplift, Tazhong Uplift Guchengxu Uplift) has reached the dry-gas generation stage. The Xishanbulake–Xidashan source rock (equivalent to the Yuertusi source rock) of well YL1 in the Kongquehe Slope shows a relatively low maturity of 1.1–1.3% and remains in the oil generation stage in the present-day. Zhu et al. (2014) reported that the Lower Cambrian R_{equ} data of the Well XH1 ranges from 1.38 to 1.55%, indicating that the Yuertusi Formation source rock in the Tabei Uplift remains in the high-mature stage and can generate petroleum or condensate gas at present. Due to the limits of drilling technology and expense, the wells in northern Shuntuoguole Low-Uplift (Shunbei Area) were drilled only to the Middle Ordovician formations at depths of 7500–7700 m. For Well SB5, the R_{equ} of the Upper Ordovician is just 0.7–0.8%.

According to the burial histories and paleo-heat flow histories (Fig. 10a and 10b; Li et al., 2010, 2022), we calculated the temperature histories of the Lower Cambrian Yuertusi Formation source rock in the Tabei Uplift (Well TS1) and Shunbei Area (Well SB5) and Upper Cambrian in the Tazhong Uplift (Well ZS1) (Fig. 10c), which have presently reached the highest temperatures of 160–185 °C along with the rapid subsidence during the Late Cenozoic, and could result in gas generation and crude oil cracking. The combination of the new gold-cube thermal simulation experiment and chemical kinetics modeling revealed that the in the Ordovician oil reservoirs in the Shunbei Area can be preserved up to ~ 180 ℃ (Fig. 10d; Li et al., 2021). Li et al. (2022) considered that the Ordovician Yijianfang and Yingshan reservoirs in the Shunbei Area just experienced the highest temperatures of 150-163℃. Therefore, there is great potential for further petroleum exploration of the deep formation in the Tabei Uplift and Shunbei Area (Fig. 1b), as evidenced by the discovered the oil fields (Yun and Zhai, 2008; Wang et al., 2014; Jiao, 2018).

6. Conclusions

The single-grain ZHe ages of the rocks in the Tarim Basin range from 94.4 Ma to 995.4 Ma with an obvious dispersion. The thermal histories revealed by forward and inverse modeling effectively constrained the highest temperature (160–180 °C) and cooling time and magnitude experienced by the rocks since the Neoproterozoic. The closure of the Proto-Tethys Ocean and South Tianshan Ocean in the Paleozoic and the collisions of the Eurasian plate with the Qiangtang terrane, Dras–Kohistan arc and India plate in the Mesozoic and Cenozoic should be responsible for the multiple tectonic cooling events occurred in the Tarim Basin. The unique thermal histories of sedimentary rocks in the Tabei Uplift and Shunbei area may indicate a great potential for further petroleum exploration at the depth below 8000 m.

CRediT authorship contribution statement

Jian Chang: Conceptualization, Data curation, Formal analysis, Methodology, Project administration, Supervision. **Xin Yang:** . **Nansheng Qiu:** . **Kyoungwon Min:** . **Chenxing Li:** Software, Visualization. **Huili Li:** . **Dan Li:** Data curation.

References

Alexeiev, D.V., Biske, Y.S., Djenchuraeva, A.V., Kröner, A., Getman, O.F., 2019. Late Carboniferous (Kasimovian) closure of the South Tianshan Ocean: no triassic subduction. J. Asian Earth Sci. 173, 54–60.

Anderson, A.J., Hodges, K.V., van Soest, M.C., 2017. Empirical constraints on the effects of radiation damage on helium diffusion in zircon. Geochim. Cosmochim. Acta 218, 308–322. https://doi.org/10.1016/j.gca.2017.09.006.

Bosboom, R., Dupont-Nivet, G., Grothe, A., Brinkhuis, H., Villa, G., Mandic, O., Stoica, M., Kouwenhoven, T., Huang, W., Yang, W., Guo, Z., 2014. Timing, cause and impact of the late Eocene stepwise sea retreat from the Tarim Basin (west China). Palaeogeogr. Palaeoclimatol. Palaeoecol. 403, 101–118. https://doi.org/10.1016/j.palaeo.2014.03.035.

Buslov, M.M., Klerkx, J., Abdrakhmatov, K., Delvaux, D., Batalev, V.Y., Kuchai, O.A., Dehandschutter, B., Muraliev, A., 2003. Recent strike-slip deformation of the northern Tianshan. In: Storti, F., Holdsworth, R.E., Salvini, F. (Eds.), Intraplate Strike-slip Deformation Belts. Geological Society London, vol. 210, pp. 53-64.

Carrapa, B., DeCelles, P.G., Wang, X., Clementz, M.T., Mancin, N., Stoica, M., Kraatz, B., Meng, J., Abdulov, S., Chen, F., 2015. Tectono-climatic implications of Eocene Paratethys regression in the Tajik basin of central Asia. Earth Planet. Sci. Lett. 424, 168–178. https://doi.org/10.1016/j.epsl.2015.05.034.

Chang, J., Brown, R.W., Yuan, W.M., Li, W.Z., Que, Y.Q., Qiu, N.S., 2014. Mesozoic cooling history of the "Bachu Uplift" in the Tarim Basin, China: Constraints from zircon fission-track thermochronology. Radiat. Meas. 67, 5–14.

Chang, J., Li, D., Min, K., Qiu, N.S., Xiao, Y., Wu, H., Liu, N., 2019. Cenozoic deformation of the Kalpin fold-and-thrust belt, southern Chinese Tian Shan: New insights from low-T thermochronology and sandbox modeling. Tectonophysics 766, 416–432.

Chang, J., Qiu, N., Li, C., Zhang, J., Li, W., Fu, X., 2022. Zircon He diffusion kinetics models and its implications on the thermal history reconstruction of the ancient strata in the craton basins. China. Chinese J. Geophys. 65 (2), 711–725 in Chinese with English abstract.

Chang, J., Qiu, N., Li, J., 2012a. Tectono-thermal evolution of the northwestern edge of the Tarim Basin in China: Constraints from apatite (U–Th)/He thermochronology. J. Asian Earth Sci. 61, 187–198. https://doi.org/10.1016/j.jseaes.2012.09.020.

Chang, J., Qiu, N., Li, J., 2012b. U-Pb dating of detrital zircon from Lower Silurian in Keping Area of Tarim Basin and its geological implication. Journal of Earth Sciences and Environment. 34 (3), 22–33.

Chang, J., Qiu, N.S., Song, X.Y., Li, H.L., 2016. Multiple cooling episodes in the Central Tarim (Northwest China) revealed by apatite fission track analysis and vitrinite reflectance data. Int. J. Earth Sci. 105 (4), 1257–1272.

Chang, J., Qiu, N.S., Zuo, Y.H., Li, C.C., 2011. The new evidence on tectonic uplift in Kepingtage area, Tarim, China: Constraints from (U-Th)/He ages. Chinese Journal of Geophysics-Chinese Edition 54 (1), 163–172. https://doi.org/10.3969/j.issn.0001-5733.2011.01.017.

Chang, J., Tian, Y.T., Qiu, N.S., 2017. Mid-Late Miocene deformation of the northern Kuqa fold-and-thrust belt (southern Chinese Tian Shan): An apatite (U-Th-Sm)/He study. Tectonophysics 694, 101–113.

Chen, Y., Yan, W., Han, C., Yan, L., Ran, Q., Kang, Q., He, H., Ma, Y., 2019. Structural and sedimentary basin transformation at the Cambrian/Neoproterozoic interval in Tarim Basin: implication to subsalt dolostone exploration. Natural Gas Geoscience 30 (1), 39–50 in Chinese with English abstract.

Chen, Y., Yan, W., Han, C., Yang, P., Li, Z., 2015. Redefinition on structural paleogeography and lithofacies paleogeography framework from Cambrian to Early Ordovician in the Tarim Basin: a new approach based on seismic stratigraphy evidence. Natural Gas Geoscience 26 (10), 1831–1843 in Chinese with English abstract.

Clift, P.D., Carter, A., Jonell, T.N., 2014. U-Pb dating of detrital zircon grains in the Paleocene Stumpata Formation, Tethyan Himalaya, Zanskar, India. J. Asian Earth Sci. 82, 80–89. https://doi.org/10.1016/j.jseaes.2013.12.014.

DeLucia, M.S., Guenthner, W.R., Marshak, S., Thomson, S.N., Ault, A.K., 2018. Thermochronology links denudation of the Great Unconformity surface to the supercontinent cycle and snowball Earth. Geology 46 (2), 167–170. https://doi.org/10.1130/G39525.1.

Deng, S., Li, H., Zhang, Z., Zhang, J., Yang, X., 2019. Structural characterization of intracratonic strike-slip faults in the central Tarim Basin. AAPG Bull. 103 (1), 109–137. https://doi.org/10.1306/06071817354.

Dumitru, T.A., Zhou, D., Chang, E.Z., Graham, S.A., Hendrix, M.S., Sobel, E.R., Carroll, A. R., 2001. Uplift, exhumation, and deformation in the Chinese Tian Shan. Geol. Soc. Am. Mem. 194, 71–99.

Farley, K.A., Wolf, R.A., Silver, L.T., 1996. The effects of long alpha-stopping distances on U-Th-He ages. Geochim. Cosmochim. Acta 60 (21), 4223–4229.

Ge, R., Zhu, W., Wilde, S.A., He, J., Cui, X., Wang, X., Bihai, Z., 2014. Neoproterozoic to Paleozoic long-lived accretionary orogeny in the northern Tarim Craton. Tectonics 33 (3), 302–329. https://doi.org/10.1002/2013tc003501.

Geisler, T., Pidgeon, R.T., 2002. Raman scattering from matamict zircon: comments on "Metamictisation of natural zircon: accumulation versus thermal annealing of radioactivity-induced damage". Contrib. Miner. Petrol. 141, 125–144.

Gleadow, A., Harrison, M., Kohn, B., Lugo-Zazueta, R., Phillips, D., 2015. The Fish Canyon Tuff: A new look at an old low-temperature thermochronology standard. Earth Planet. Sci. Lett. 424, 95–108. https://doi.org/10.1016/j.epsl.2015.05.003.

Glorie, S., De Grave, J., Buslov, M.M., Zhimulev, F.I., Stockli, D.F., Batalev, V.Y., Izmer, A., Van den haute, P., Vanhaecke, F., Elburg, M. A., 2011. Tectonic history of the Kyrgyz South Tien Shan (Atbashi-Inylchek) suture zone: The role of inherited structures during deformation-propagation. Tectonics, 30(6), doi:10.1029/2011tc002949.

Green, P., Duddy, I., 2018. Apatite (U-Th-Sm)/He thermochronology on the wrong side of the tracks. Chem. Geol. 488, 21–33. https://doi.org/10.1016/j.chemgeo.2018.04.028.

Guenthner, W.R., Reiners, P.W., DeCelles, P.G., Kendall, J., 2015. Sevier belt exhumation in central Utah constrained from complex zircon (U-Th)/He data sets: Radiation damage and He inheritance effects on partially reset detrital zircons. Geol. Soc. Am. Bull. 127 (3–4), 323–348. https://doi.org/10.1130/B31032.1.

Guenthner, W.R., Reiners, P.W., Drake, H., Tillberg, M., 2017. Zircon, titanite, and apatite (U-Th)/He ages and age-eU correlations from the Fennoscandian Shield, southern Sweden. Tectonics 36 (7), 1254–1274. https://doi.org/10.1002/2017tc004525.

Guenthner, W.R., Reiners, P.W., Ketcham, R.A., Nasdala, L., Giester, G., 2013. Helium diffusion in natural zircon: Radiation damage, anisotropy, and the interpretation of zircon (U-Th)/He thermochronology. Am. J. Sci. 313 (3), 145–198. https://doi.org/10.2475/03.2013.01.

Guo, C., Gao, J., Li, Z., Zhang, L., 2017. Depositional and provenance records of Upper Devonian to Lower Carboniferous sandstones from Bachu Area, Northwestern Tarim Basin: implications for tectonic evolution. Earth Sci. 42 (3), 421–434 in Chinese with English abstract.

Guo, S., Hong, K., 2007. Silurian-Devonian sequence stratigraphy and favorable reservoir distribution in Tarim Basin. Acta Petrolei Sinica 28 (3), 44–50 in Chinese with English abstract.

Han, B.F., He, G.Q., Wang, X.C., Guo, Z.J., 2011. Late Carboniferous collision between the Tarim and Kazakhstan-Yili terranes in the western segment of the South Tian Shan Orogen, Central Asia, and implications for the Northern Xinjiang, western China. Earth Sci. Rev. 109 (3–4), 74–93. https://doi.org/10.1016/j.earscirev.2011.09.001.

Han, Y., Zhao, G., 2018. Final amalgamation of the Tianshan and Junggar orogenic collage in the southwestern Central Asian Orogenic Belt: Constraints on the closure of the Paleo-Asian Ocean. Earth Sci. Rev. 186, 129–152. https://doi.org/10.1016/j.earscirev.2017.09.012.

He, D., Jia, C., Li, D., Zhang, C., Meng, Q., Shi, X., 2005. Formation and evolution of polycyclic superimposed Tarim Basin. Oil Gas Geol. 26, 64–77 in Chinese with English abstracts.

He, J., Wu, G., Xu, B., Qu, T., Li, H., Cao, Y., 2010. Characteristics and petroleum exploration significance of unconformity between Sinian and Cambrian in Tarim Basin. Chinese Journal of Geology 45 (3), 698–706 in Chinese with English abstract.

Jacob, H., 1989. Classification, structure, genesis and practical importance of natural solid bitumen. Int. J. Coal Geol. 11, 65–79.

Jia, C., 1997. Tectonics characteristics of the Tarim Basin in China and its oil-gas resources. Petroleum Industry Press, Beijing.

Jiao, F., 2018. Significance and prospect of ultra-deep carbonate fault-karst reservoirs in Shunbei Area. Tarim Basin. Oil & gas Geology 39 (2), 207–216 in Chinese with English abstract.

Johnson, J.E., Flowers, R.M., Baird, G.B., Mahan, K.H., 2017. "Inverted" zircon and apatite (U–Th)/He dates from the Front Range, Colorado: High-damage zircon as a low-temperature (<50 °C) thermochronometer. Earth Planet. Sci. Lett. 466, 80–90. https://doi.org/10.1016/j.epsl.2017.03.002.

Jolivet, M., 2015. Mesozoic tectonic and topographic evolution of Central Asia and Tibet: a preliminary synthesis. Geological Society, London, Special Publications. https://doi.org/10.1144/sp427.2.

Jonckheere, R., Heinz, D., Hacker, B.R., Rafaja, D., Ratschbacher, L., 2019. A borehole investigation of zircon radiation damage annealing. Terra Nova 31 (3), 263–270. https://doi.org/10.1111/ter.12395.

Ketcham, R.A., 2005. Forward and Inverse Modeling of Low-Temperature Thermochronometry Data. Rev. Mineral. Geochem. 58 (1), 275–314. https://doi.org/10.2138/rmg.2005.58.11.

Li, D., Chang, J., Qiu, N., Wang, J., Zhang, M., Wu, X., Han, J., Li, H., Ma, A., 2022. The thermal evolution history in sedimentary basins: A case study of the central Tarim Basin, Western China, Journal of Asian Earth Sciences, revised.

Li, H., Qiu, N., Jin, Z., He, Z., 2005. Geothermal history of Tarim Basin. Oil Gas Geol. 26, 613–617 in Chinese with English abstract.

Li, H.L., Ma, A.L., Cai, X.Y., Lin, H.X., Li, J.J., Liu, J.Z., Zhu, X.X., Wu, X., 2021. Kinetics of oil-cracking of ultra-deep Ordovician oil in the North Shuntuoguole area of Tarim Basin and its geological implications. Petroleum Geology & Experiment 43 (5), 818–825 in Chinese with English abstract.

Li, J., Zhou, X., Li, W., Wang, H., Liu, Z., Zhang, H., Ta, S., 2015a. Preliminary reconstruction of tectonic paleogeography of Tarim Basin and its adjacent areas from Cambrian to Triassic. NW China. Geological Review 61 (6), 1225–1234 in Chinese with English abstract.

Li, M., Wang, T., Chen, J., He, F., Yun, L., Akbar, S., Zhang, W., 2010. Paleo-heat flow evolution of the Tabei Uplift in Tarim Basin, northwest China. J. Asian Earth Sci. 37 (1), 52–66. https://doi.org/10.1016/j.jseaes.2009.07.007.

Li, S.Z., Zhao, S.J., Liu, X., Cao, H.H., Yu, S., Li, X.Y., Somerville, I., Yu, S.Y., Suo, Y.H., 2018. Closure of the Proto-Tethys Ocean and Early Paleozoic amalgamation of microcontinental blocks in East Asia. Earth-Sci. Rev. 186, 37–75.

Li, Y.Q., Li, Z.L., Sun, Y.L., Santosh, M., Langmuir, C.H., Chen, H.L., Yang, S.F., Chen, Z. X., Yu, X., 2012. Platinum-group elements and geochemical characteristics of the Permian continental flood basalts in the Tarim Basin, northwest China: Implications for the evolution of the Tarim Large Igneous Province. Chem. Geol. 328, 278–289.

Li, Z., Qiu, N.S., Chang, J., Yang, X.M., 2015b. Precambrian evolution of the Tarim Block and its tectonic affinity to other major continental blocks in China: New clues from U-Pb geochronology and Lu-Hf isotopes of detrital zircons. Precambr. Res. 270, 1–21.

Li, Z.L., Chen, H.L., Song, B.A., Li, Y.Q., Yang, S.F., Yu, X., 2011. Temporal evolution of the Permian large igneous province in Tarim Basin in northwestern China. J. Asian Earth Sci. 42 (5), 917–927.

Lin, C., Yang, H., Liu, J., Rui, Z., Cai, Z., Zhu, Y., 2012. Distribution and erosion of the Paleozoic tectonic unconformities in the Tarim Basin, Northwest China: Significance for the evolution of paleo-uplifts and tectonic geography during deformation. J. Asian Earth Sci. 46, 1–19. https://doi.org/10.1016/j.jseaes.2011.10.004.

Liu, D.H., Shi, J.Y., 1994. Study on the evaluation methods on high matured carbonate source rocks. Pet. Explor. Dev. 21, 113–115.

Liu, S., Lei, X., Feng, C., Hao, C., 2016. Estimation of subsurface formation temperature in the Tarim Basin, northwest China: implications for hydrocarbon generation and preservation. Int. J. Earth Sci. https://doi.org/10.1007/s00531-015-1253-4.

Morin, J., Jolivet, M., Barrier, L., Laborde, A., Li, H., Dauteuil, O., 2019. Planation surfaces of the Tian Shan Range (Central Asia): Insight on several 100 million years of topographic evolution. J. Asian Earth Sci. 177, 52–65. https://doi.org/10.1016/j.jseaes.2019.03.011.

Orme, D.A., Guenthner, W.R., Laskowski, A.K., Reiners, P.W., 2016. Long-term tectonothermal history of Laramide basement from zircon-He age-eU correlations. Earth Planet. Sci. Lett. 453, 119–130. https://doi.org/10.1016/j.epsl.2016.07.046.

Powell, J., Schneider, D.P., Stockli, D., Fallas, K., 2016. Zircon (U-Th)/He thermochronology of Neoproterozoic strata from the Mackenzie Mountains, Canada: Implications for the Phanerozoic exhumation and deformation history of the northern Canadian Cordillera. Tectonics 35, 663–689.

Qiu, H., Deng, S., Cao, Z., Yin, T., Zhang, Z., 2019. The Evolution of the Complex Anticlinal Belt With Crosscutting Strike-Slip Faults in the Central Tarim Basin. NW China. Tectonics 38 (6), 2087–2113. https://doi.org/10.1029/2018tc005229.

Qiu, N., Chang, J., Zuo, Y., Wang, J., Li, H., 2012. Thermal evolution and maturation of lower Paleozoic source rocks in the Tarim Basin, northwest China. AAPG Bull. 96 (5), 789–821. https://doi.org/10.1306/09071111029.

Qiu, N., Wang, J., Mei, Q., Jiang, G., Tao, C., 2010. Constraints of (U-Th)/He ages on early Paleozoic tectonothermal evolution of the Tarim Basin. China. Science China Earth Sciences 53 (7), 964–976. https://doi.org/10.1007/s11430-010-4004-1.

Reiners, P.W., Stefan, U., 2006. Measurement of parent nuclides for (U-Th)/He chronometry by solution sector ICP-MS. ARHDL Report 1.

Ren, Z., Xiao, H., Han, W., Liang, Y., Qing, Y., Teng, Z., Shi, Z., 2009. Research on basin-mountain tectonic-thermal history of Kongquehe Slope and Kuruketag Uplift. Journal of Northwest University (Natural Science Edition) 39 (3), 510–516 in Chinese with English abstract.

Robinson, A.C., Yin, A., Manning, C.E., Harrison, T.M., Zhang, S.H., Wang, X.F., 2004. Tectonic evolution of the northeastern Pamir: Constraints from the northern portion of the Cenozoic Kongur Shan extensional system, western China. GSA Bulletin 116 (7), 953–973. https://doi.org/10.1130/b25375.1.

Shao, L., He, Z., Gu, J., Luo, W., Jia, J., Liu, Y., Zhang, L., Zhang, P., 2006. Lithofacies palaeogeography of the Paleogene in Tarim Basin. J. Palaeogeogr. 8 (3), 353–364 in Chinese with English abstract.

Sobel, E.R., 1999. Basin analysis of the Jurassic-Lower Cretaceous southwest Tarim basin, northwest China. GSA Bulletin 111, 709–724.

Sun, J., Windley, B.F., Zhang, Z., Fu, B., Li, S., 2016a. Diachronous seawater retreat from the southwestern margin of the Tarim Basin in the late Eocene. J. Asian Earth Sci. 116, 222–231. https://doi.org/10.1016/j.jseaes.2015.11.020.

Sun, J., Xiao, W., Windley, B.F., Ji, W., Fu, B., Wang, J., Jin, C., 2016b. Provenance change of sediment input in the northeastern foreland of Pamir related to collision of the Indian plate with the Kohistan-Ladakh arc at around 47 Ma. Tectonics, n/a-n/a. https://doi.org/10.1002/2015tc003974.

Sun, J., Zhang, Z., Cao, M., Windley, B.F., Tian, S., Sha, J., Abdulov, S., Gadoev, M., Oimahmadov, I., 2020. Timing of seawater retreat from proto-Paratethys, sedimentary provenance, and tectonic rotations in the late Eocene-early Oligocene in the Tajik Basin, Central Asia. Palaeogeogr. Palaeoclimatol. Palaeoecol. 545 https://doi.org/10.1016/j.palaeo.2020.109657.

Wang, L., Li, C., Shi, Y., 1995. Distribution of terrestrial heat flow density in Tarim Basin. Western China. Acta Geophysica Sinica 38 (6), 855–856 in Chinese.

Wang, Z., Xie, H., Chen, Y., Qi, Y., Zhang, K., 2014. Discovery and exploration of Cambrian subsalt dolomite original hydrocarbon reservoir at Zhongshen-1 Well in Tarim Basin. China Petroleum Exploration 19 (2), 1–13 in Chinese with English abstract.

Wolfe, M.R., Stockli, D.F., 2010. Zircon (U–Th)/He thermochronometry in the KTB drill hole, Germany, and its implications for bulk He diffusion kinetics in zircon. Earth Planet. Sci. Lett. 295 (1–2), 69–82. https://doi.org/10.1016/j.epsl.2010.03.025.

Wu, G.H., Chen, X., Ma, B.S., Chen, Y.Q., Tian, W.Z., Huang, S.Y., Feng, X.J., 2021. The tectonic environments of the Late Neoproterozoic-Early Paleozoic and its tectono-sedimentary response in the Tarim Basin. Acta Petrologica Sinica 37 (8), 2431–2441 in Chinese with English abstract.

Wu, G.H., Deng, W., Huang, S.Y., Zheng, D.M., Pan, W.Q., 2020. Tectonic-paleogeographic evolution in the Tarim Basin. Chinese Journal of Geology 55 (2), 305–321 in Chinese with English abstract.

Wu, L., Guan, S., Zhang, S., Yang, H., Jin, J., Zhang, X., Zhang, C., 2018. Neoproterozoic stratigraphic framework of the Tarim Craton in NW China: Implications for rift evolution. J. Asian Earth Sci. 158, 240–252. https://doi.org/10.1016/j.jseaes.2018.03.003.

Xiao, X.M., Wilkins, R.W.T., Liu, D.H., Liu, Z.F., Fu, J.M., 2000. Investigation of thermal maturity of lower Paleozoic hydrocarbon source rocks by means of vitrinite like maceral reflectance: A Tarim Basin case study. Org Geochem. 31, 1041–1052.

Xu, Y., Wei, X., Luo, Z., Liu, H., Cao, J., 2014. The Early Permian Tarim Large Igneous Province: Main characteristics and a plume incubation model. Lithos 204, 20–35. https://doi.org/10.1016/j.lithos.2014.02.015.

Xu, Z., He, B., Zhang, C., Zhang, J., Wang, Z., Cai, Z., 2013. Tectonic framework and crustal evolution of the Precambrian basement of the Tarim Block in NW China: New geochronological evidence from deep drilling samples. Precambr. Res. 235, 150–162. https://doi.org/10.1016/j.precamres.2013.06.001.

Yang, H., 2015. Exploration knowledge and direction of Lower Proterozoic inner dolostones. Tarim Basin. Natural Gas Geoscience 26 (7), 1213–1223 in Chinese with English abstract.

Yang, W., Niu, H., Shan, Q., Luo, Y., Sun, W., Li, C., Li, N., Yu, X., 2012. Late Paleozoic calc-alkaline to shoshonitic magmatism and its geodynamic implications, Yuximolegai area, western Tianshan. Xinjiang. Gondwana Research 22 (1), 325–340. https://doi.org/10.1016/j.gr.2011.10.008.

Yang, X., Li, H., Yue, Y., Liu, S., Li, J., Xiong, P., 2017. The strata and paleo-geomorphology framework at the end of Neoproterozoic and development mode of source rocks at the beginning of Cambrian. Natural Gas Geoscience 28 (2), 189–198 in Chinese with English abstract.

Yang, Y., Liu, J., Tian, J., Meng, W., Zhang, X., Zhu, H., 2011. Sequence lithofacies paleogeography of Cambrian in Tarim Basin. Natural Gas Geoscience 22 (3), 450–459 in Chinese with English abstract.

Yin, A., Harrison, T.M., 2000. Geologic evolution of the Himalayan-Tibetan Orogen. Annu. Rev. Earth Planet. Sci. 28, 211–280.

Yun, J., Jin, Z., Xie, G., 2014. Distribution of major hydrocarbon source rocks in the Lower Paleozoic. Tarim Basin. Oil & gas Geology 35 (6), 827–838 in Chinese with English abstract.

Yun, L., Zhai, X., 2008. Discussion on characteristics of the Cambrian reservoirs and hydrocarbon accumulation in Well Tashen-1. Tarim Basin. Oil & gas Geology 29 (6), 726–732 in Chinese with English abstract.

Zhang, C., Jia, C., Li, B., Luo, X., Liu, Y., 2010. Ancient karsts and hydrocarbon accumulation in the middle and western parts of the North Tarim uplift. NW China. Petroleum Exploration and Development 37 (3), 263–269 in Chinese with English abstract.

Zhang, C., Zheng, D., Li, J., 2001. Attribute of Paleozoic structures and its evolution characteristics in Kalpin fault-uplift. Oil Gas Geol. 22 (4), 314–318 in Chinese with English abstracts.

Zhang, C., Zou, H., Li, H., Wang, H., 2013. Tectonic framework and evolution of the Tarim Block in NW China. Gondwana Res. 23 (4), 1306–1315. https://doi.org/10.1016/j.gr.2012.05.009.

Zhang, G., 2000. The formation and evolution of the Tarim cratonic basin in Paleozoic and its hydrocarbon. Geological publishing house, Beijing.

Zhang, J., Yu, S., Mattinson, C., 2017. Early Paleozoic polyphase metamorphism in northern Tibet, China. Gondwana Res. 41, 267–289.

Zhang, S., Liu, J., Tian, J., Zhao, X., He, J., 2004. Factors influencing sandstone reservoir quality in Donghetang Formation, Tarim Basin, China. Journal of Chengdu University of Technology (Science & Technology Edition) 31 (6), 658–662 in Chinese with English abstract.

Zhang, X., Tian, J., Peng, J., 2008. The lithofacies-paleogeography and space-time evolvement of Silurian-Devonian in the Tarim Basin. Acta Sedimentlogica Sinica 26 (5), 762–771 in Chinese with English abstract.

Zhang, Y., He, D., Liu, C., 2019. Three-dimensional geological structure and genetic mechanism of the Bachu uplift in the Tarim Basin. Earth Sci. Front. 26 (1), 134–148 in Chinese with English abstract.

Zhang, Z., Zhu, W., Shu, L., Wan, J., Yang, W., Zheng, B., Su, J., 2011. Multi-stage exhumation of the NE Tarim Precambrian bedrock, NW China: constraints from apatite fission track thermochronology in the Kuluketage area. Terra Nova 23 (5), 324–332. https://doi.org/10.1111/j.1365-3121.2011.01017.x.

Zheng, X., 2016. The faulting characteristics and paleo-uplift migration of Bachu uplift, Tarim Basin. PhD thesis, Zhejiang University.

Zheng, X., He, G., Yao, Z., 2016. Structural characteristics and geometric models of the Yasongdi Fault Belt, the Bachu Uplift. Earth Sci. Front. 23 (4), 255–264 in Chinese with English abstract.

Zhu, C., Yan, H., Yun, L., Han, Q., Ma, H., 2014. Characteristics of Cambrian source rocks in well XH1, Shaya Uplift. Tarim Basin. Petroleum Geology & Experiment 36 (5), 626–632 in Chinese with English abstract.

Zhu, G.Y., Ren, R., Chen, F.R., Li, T.T., Chen, Y.Q., 2017. Neoproterozoic rift basins and their control on the development of hydrocarbon source rocks in the Tarim Basin, NW China. J. Asian Earth Sci. 150, 63–72. https://doi.org/10.1016/j.jseaes.2017.09.018.